RESEARCH ARTICLE

ADVANCED MATERIALS
www.advmat.de

Dimensionally Stable Nanofibrous Nonwoven as a Flexible Dynamic Emissivity Switching Temperature-Regulating Material

Eva Loccufier, Muluneh G. Abebe, Jozefien Geltmeyer, Timo Meirman, Ozlem Ipek Kalaoglu Altan, Joachim F. R. Van Guyse, Eric Khousakoun, Hayriye Gidik, Elham Mohsenzadeh, Driss Lahem, Richard Hoogenboom, Bjorn Maes, and Karen De Clerck**

Smart textiles that passively regulate thermal comfort provide a sustainable alternative to energy-intensive climate control. A promising strategy involves modulating radiative heat transfer by dynamically adjusting surface emissivity, thereby facilitating reversible switching between heat-retentive and heat-dissipative states. Existing systems enable emissivity switching but often need external energy or lack dimensional stability when deformed, which limits wearable applications. Here, a fully passive, autonomously adaptive dynamic emissivity switch textile (DEST) based on a thermo- and humidity-responsive electrospun poly(*N*-isopropyl acrylamide) (PNIPAM) copolymer is introduced. To ensure robust functionality in humid or aqueous environments, a crosslinkable allyl-functionalized PNIPAM copolymer is synthesized via post-polymerization amidation of a P(NIPAM-*co*-methyl acrylate) copolymer and processed using a green water-ethanol-based electrospinning technique. Thiol-ene crosslinking produced water-stable, thermoresponsive nanofibers with a transition near skin temperature. For reversible macropore actuation, a dimensionally stable architecture is employed that avoids out-of-plane distortion, achieved through a honeycomb-shaped electrospinning collector and a tailored mechanical cutting pattern. A silver coating imparts the overall infrared (IR) reflectivity, facilitating radiative heat retention when the macropores are closed. The resulting DEST exhibits dual responsiveness to temperature and ambient humidity, enabling passive switching between emissive and reflective states without external energy input, with a ≈6 °C reversible thermal comfort window.

1. Introduction

Maintaining thermal comfort in both living and working environments is crucial for human well-being, productivity, and overall health. With rising global temperatures and the growing need for climate control, the demand for efficient thermal regulation is poised to intensify. Currently, thermal comfort is predominantly achieved through centralized heating, ventilation, and air conditioning systems, which together account for over 20% of the global energy consumption.[1,2] These active forms of thermal regulation place considerable strain on energy infrastructure, particularly in densely populated areas and areas with extreme climates.

An emerging strategy to reduce the reliance on the energy-intensive thermal regulation of infrastructure is the development of materials that regulate personal thermal comfort.[3,4] Among these, smart textiles that can adapt their thermal properties to external conditions offer a promising route to localized, energy-passive thermal regulation. By dynamically modulating infrared (IR) emissivity, these textiles can switch between heat-retaining (low emissivity) and heat-releasing (high emissivity)

E. Loccufier, J. Geltmeyer, T. Meirman, K. De Clerck
Centre for Textile Science and Engineering (CTSE)
Department of Materials
Textiles and Chemical Engineering
Ghent University
Technologiepark 70A, Ghent 9052, Belgium
E-mail: Eva.Loccufier@UGent.be; Karen.DeClerck@UGent.be

The ORCID identification number(s) for the author(s) of this article can be found under https://doi.org/10.1002/adma.202517161

DOI: 10.1002/adma.202517161

M. G. Abebe, B. Maes
Micro- and Nanophotonic Materials Group
Research Institute for Materials Science and Engineering
University of Mons
20 Place du Parc, Mons B-7000, Belgium

O. I. K. Altan
Faculty of Textile Technologies and Design
Department of Textile Engineering
Istanbul Technical University
Inonu Cad No: 65, Beyoglu, Istanbul 34437, Turkey

states, depending on the wearer's needs and the surrounding environment.[5,6] Better known as dynamic emissivity switch textiles (DESTs), these systems are designed to mimic biological principles used by squids and lizards to passively regulate thermal comfort.[7–11] In addition, the porous structure of fabrics enables designs that allow for both moisture regulation and heat regulation, another important factor in maintaining a comfortable body temperature.[4,12–17]

DESTs can be both active and passive, depending on the stimuli that enable the thermal regulation.[6,18–25] Active materials, such as those driven by electrical power, regulate heat exchange, thereby reducing energy consumption,[1] but only a few fast-switching dual-mode thermal regulating textiles exist.[26] Although these can lead to practical actuation problems, energy consumption can be minimized by using alternative external stimuli, such as mechanical pressure.[24,25] Even then, fast-responsive passive thermal regulating materials are favored. However, the currently available materials have significant limitations in both material properties and performance, including mechanical instability or deformation during actuation, the need for manual switching (flip-over designs), a lack of biocompatibility and eco-friendly fabrication, and a limited thermal or ambient humidity operating range.[1,7,8,10,15,18,21–34]

A recently investigated method to enhance the response time of thermoregulating materials is the use of electrospun nanofibers. Compared to conventional textile production methods, electrospinning produces fibers with nanometer-scale diameters, resulting in a very high specific surface area.[35] Combined with the large porosity in between the fibers, the overall fabric has the potential for a significantly faster response and, thus, a quicker thermal regulation.[36–40] Additionally, the combination of these properties enables significant potential changes in the fabric's dimensions in response to thermal stimuli.

The development of thermally regulating textiles comprising electrospun nanofibers has been reported over the last five years for use in, e.g., all-weather smart textiles, air-conditioned masks, and sun blinds for windows.[14,38,40–48] These have focused on enhancing thermal management capabilities through innovative material compositions, for example, by incorporating polyethylene glycol as a phase-change material into the electrospinning solution.[49,50] However, there is a shortage of materials that simultaneously address the use of a green electrospinning process, the material's biocompatibility and environmental sustainability, and incorporate a layer that guarantees dimensional stability during pore opening/closing.[28,29,39,51–53]

Therefore, we developed a new textile structure consisting of a thermo- and humidity-responsive electrospun poly(*N*-isopropyl acrylamide) (PNIPAM) copolymer coated with silver (Ag) nanoparticles as a textile coating layer that exhibits a fast and reversible thermal response (**Figure 1**). PNIPAM is a thermoresponsive polymer with a lower critical solution temperature (LCST) of ≈32 °C in water. Below this temperature, it becomes water-soluble, enabling a green electrospinning process using an aqueous ethanol solution. In addition to its high functionalization potential—which allows for tailoring the water stability of electrospun PNIPAM fibers through crosslinking (later referred to as PNIPAM-X)—PNIPAM and its copolymers have been extensively studied and are widely recognized for their biocompatibility.[54–58] Numerous in vitro and in vivo studies have demonstrated their low cytotoxicity and suitability for biomedical applications such as drug delivery, tissue engineering, and regenerative medicine. For instance, PNIPAM-based hydrogels have shown excellent compatibility with mammalian cells and have been used as scaffolds for cell culture and tissue regeneration.[59] Moreover, copolymers, such as dextran-grafted PNIPAM, have been shown to enhance the cytotoxicity of chemotherapeutic agents while maintaining biocompatibility.[60–62] The resulting nonwoven therefore shows strong potential for application in the development of smart textiles designed for skin contact. Furthermore, the design is enhanced by implementing a mechanical metamaterial inspired by zero Poisson material.[63–67] By developing a honeycomb-like configuration, the overall dimensional stability is ensured, allowing the use of this nonwoven fabric as a top layer on other materials. This concept is schematically depicted in Figure 1 for a skin-contact application, specifically a thermoregulating sports T-shirt, which serves as the first proof-of-concept application for our DEST.

2. Results and Discussion

2.1. Model-Based Design of Dimensionally Stable Nanofibrous DEST

In this work, the proposed DEST structure consists of layered components, namely a unidirectional carbon-fiber high-emissive textile bottom layer, with a 70–100 μm thin electrospun thermoresponsive PNIPAM-X fabric coated with a 50 nm layer of silver nanoparticles on top to ensure good conductivity without loss in biocompatibility.[68–71] A carbon fiber bottom layer was chosen for proof-of-concept purposes, but any fabric with high emission can replace this, such as woven cotton fabrics with dedicated coloring.[72–75]

A functional DEST for dual-mode temperature regulation must operate in two modes: heat-retentive and dissipative. The fabric is in heat-retention mode when the ambient temperature is low. This section explains the concept in detail through modeling the effective emissivity of the proposed DEST. The added value of this DEST compared to a traditional textile and bare skin is illustrated through the thermal circuit model for the skin-textile-environment structure, which accounts for a small air gap between the textile and the skin (Figure 1). Initially, at low

---

J. F. R. Van Guyse, R. Hoogenboom
Supramolecular Chemistry Group
Centre of Macromolecular Chemistry (CMaC)
Department of Organic and Macromolecular Chemistry
Ghent University
Krijgslaan 281 S4, Ghent 9000, Belgium

E. Khousakoun, D. Lahem
Materia Nova
Materials Science Unit
3 Avenue Nicolas Copernic, Mons 7000, Belgium

H. Gidik, E. Mohsenzadeh
Univ. Lille
ENSAIT
ULR 2461 – GEMTEX-Génie et Matériaux Textiles
Lille F-59000, France

H. Gidik, E. Mohsenzadeh
Junia
Lille F-59000, France

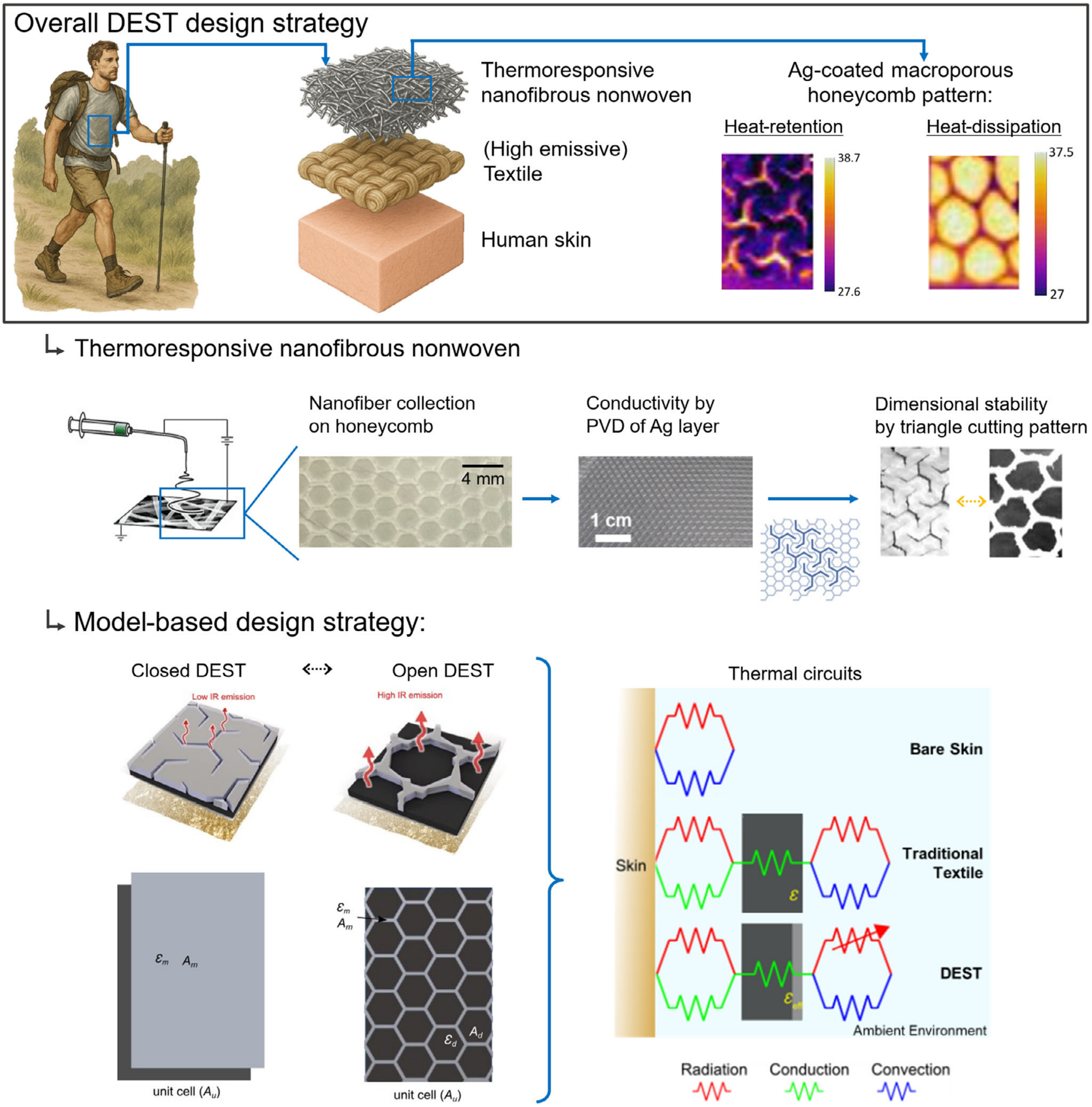

Figure 1. Model-based design strategy of a dynamic emissivity switch textile (DEST) for dual-mode temperature regulation. The DEST consists of a high-emissive textile bottom layer topped with a thermo- and humidity-responsive crosslinked electrospun PNIPAM copolymer. This nonwoven layer is coated with silver through physical vapor deposition. A macroscopic 3-legged triangle pattern is cut into the nonwoven, creating a dimensionally stable top layer that facilitates reversible opening and closing of macropores. This construction yields a multi-layered material capable of both heat retention and dissipation, as schematically depicted in the thermal circuit comparison with bare skin and a traditional textile.

relative humidity, the silver-coated PNIPAM-X layer keeps its original shape, leading to full coverage of the high-emission carbon fiber bottom layer. This significantly reduces the body's heat radiation to the environment by decreasing the effective emissivity of the fabric's outer surface, putting the DEST in heat-retention mode. When the ambient temperature rises, the fabric switches to heat-dissipation mode. The PNIPAM-X layer contracts, exposing the bottom, high-emission layer to the environment, increasing the effective emissivity of the outer surface and allowing heat to dissipate from the body into the environment. Details of the model-based fundamentals of this DEST design are schematically depicted in **Figure** 2a,b and explained in detail in Section S1 (Supporting Information). The resulting map of the effective emissivity ϵ_{eff} as a function of the metalized layer's

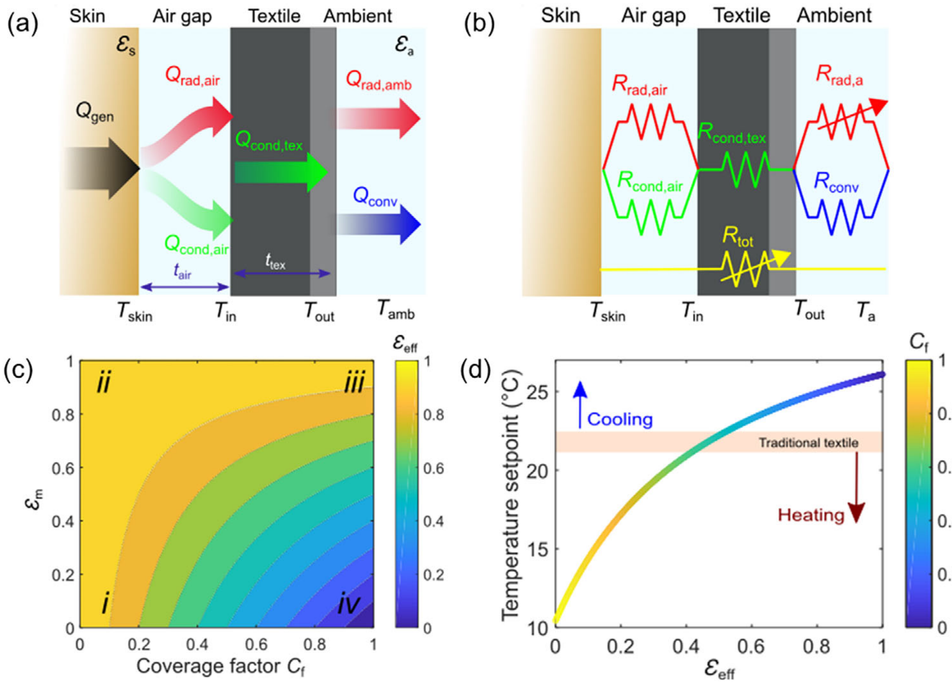

Figure 2. Analysis of the effective emissivity of a dual-layer DEST. a) Schematic representation of the main heat flow channels when the fabric covers skin, and b) the corresponding thermal circuit analogy. The resulting map of the effective emissivity ϵ_{eff} as c) a function of ϵ_m and C_f (for ϵ_d=1), and d) temperature setpoint as a function of ϵ_{eff} and C_f showcase the heating and cooling potential of the DEST.

emissivity ϵ_m and the coverage factor C_f (the metalized surface area over the bottom layer surface area), and the temperature setpoint as a function of ϵ_{eff} and C_f are given in Figure 2c,d. The effective emissivity approaches that of the metallic top layer as the C_f approaches 1. On the other hand, when the metalized islands shrink, the surface area of the top layer decreases, increasing the effective emissivity toward the theoretical limit of the bottom layer's emissivity.

The effective emissivity behavior can be categorized into four regions: i) both C_f and ϵ_m are low (bottom-left corner), ii) low C_f and high ϵ_m (top-left corner), iii) both C_f and ϵ_m are high (top-right corner), and iv) high C_f and ϵ_m low (bottom-right corner). In regions (i) and (ii), the effective emissivity remains high due to the large exposure of the bottom layer, enabling radiative cooling regardless of ϵ_m. Here, the top layer's emissivity is less critical because of its minimal coverage. Region (iii) also yields high emissivity, but through full coverage with a high-emissivity top layer. In contrast, region (iv) shows low emissivity, as the emissive bottom layer is obscured by a low-emissivity top layer, favoring heating. Thus, regions (i) and (iv) represent optimal cooling and heating scenarios, respectively, and are key targets in DEST design.

This analysis highlights the importance of minimizing the top layer's ϵ_m through precise electromagnetic design and fabrication of this layer. Thermal comfort is defined by the temperature setpoint, which is the ambient temperature at which comfort is achieved. A wider setpoint range indicates better dynamic performance. The ideal cooling setpoint reaches 26 °C (low coverage), while the heating setpoint drops to 11 °C (high coverage). For comparison, traditional fabrics like cotton exhibit only a narrow setpoint band ≈22 °C, whereas a DEST aims to expand this as much as possible. The details on these calculations are given in Section S1 (Supporting Information).

To utilize DEST technology to improve smart textiles, a flexible top layer is needed that maintains overall dimensional stability when the pores open and close in response to external stimuli. This type of mechanical metamaterial requires a specific design strategy.[55–59] Based on intensively investigated 2D re-entrant structures (e.g., chiral quadratic lattice structure, structurally hexagonal re-entrant honeycomb, square rib missing model, and lozenge missing rib model), we developed a cutting pattern to create a DEST top-layer that creates honeycomb pores upon opening and closing of the structure, see Figure 1.[56,60–62] A 3-legged triangle cutting pattern with cuts spaced 2 mm apart, as shown in **Figure 3b**, was applied to the PNIPAM-X nonwoven. To improve the opening and closing of these pores, a specialized honeycomb-shaped collector with 2 mm wide honeycombs was designed as an electrospinning collector (Figure 3a). This created areas with higher fiber density on top of the collector structure and lower fiber density in the gaps between the collector pores, as shown in the scanning electron microscopy (SEM images of Figure 3. After removal from the collector, this creates a nonwoven with localized improved mechanical stability where the honeycomb mesh collector was underneath, and larger porosity zones that are ideal for expansion and contraction when applying the cutting pattern. The local fiber-dense zones provide sufficient mechanical rigidity while maintaining flexibility, enabling reversible opening and closing of the macroscopic honeycomb pores, as shown in Section 2.4. As a result of this combined design strategy, the sample will not deform in either the lateral or axial directions while the fabric switches

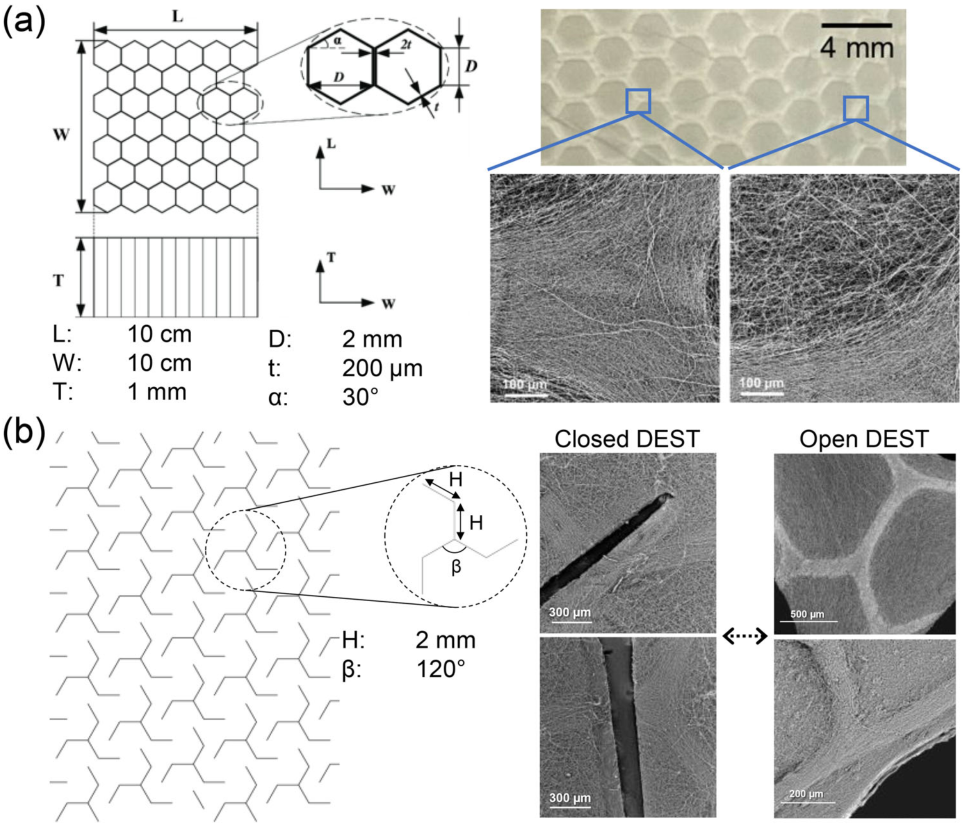

Figure 3. Shape characteristics and associated SEM images of the microstructure of a) the honeycomb aluminum electrospinning collector, and b) the 3-legged triangular cutting pattern.

between cooling and heating modes, unlike other designs. This enables an overall DEST with high flexibility, durability, and wear resistance, making it ideal for the development of smart textiles.

2.2. Thermoresponsive PNIPAM Synthesis

To develop a functionalized PNIPAM that is crosslinkable via radical thiol-ene chemistry, it was envisioned to introduce allylacrylamide comonomer units. However, copolymerization of NIPAM with allylacrylamide would lead to premature crosslinking due to radical addition to both the acrylamide and allyl groups of the latter monomer. Recently, Hoogenboom and coworkers established efficient triazabicyclodecene (TBD)-catalyzed amidation for the post-polymerization modifications of poly(methyl acrylate), including the preparation of a poly(allylacrylamide) homopolymer.[76–79] This previous work inspired the post-modification strategy for the crosslinking of PNIPAM nanofibers. Therefore, NIPAM was copolymerized with methyl acrylate to produce P(NIPAM-*co*-MA) through free radical copolymerization using 2,2′-Azobis(2-methylpropionitrile) (AIBN) as an initiator at 70 °C (**Figure 4a**). The copolymer was isolated via precipitation in diethyl ether, followed by filtration and vacuum drying. The optimal copolymer to produce water-stable nanofibers was established after a preliminary study in which the amidation ratio and the molecular weight of the polymers were varied, as shown in Section S2 (Supporting Information). The successful copolymerization was confirmed by SEC, which revealed a molecular weight (Mn) of 32.4 kDa and a dispersity (Đ) of 3.97 (Figure S2, Supporting Information). ^{1}H NMR spectroscopy was used to determine the content of methyl acrylate to be 33 mol% (Figure S2, Supporting Information). P(NIPAM-*co*-MA) was converted to P(NIPAM-*co*-AllylAm) through TBD-catalyzed amidation using allylamine (Figure 3). SEC analysis revealed an increase in Mn to 45.8 kDa and a similar Đ of 3.83, indicating that the allylacrylamide units lead to an increase in hydrodynamic volume in DMA (Figure S2, Supporting Information). The appearance of peaks at 3.7, 3.9, and 5 ppm in the ^{1}H NMR spectrum confirmed the complete transformation of the acrylate esters to allylacrylamide units in the copolymer (Figure S2, Supporting Information). The modification was further validated by the disappearance of the ester band at 1700 cm^{-1} and the appearance of the allyl band at 900 cm^{-1} in the FTIR spectra, as shown in Figure S2 (Supporting Information). The incorporation of the allyl side chains did not significantly alter the lower critical solution temperature (LCST) of the P(NIPAM-*co*-allylAm) copolymer compared to pure PNIPAM, as confirmed by cloud point measurements conducted through turbidimetry, which revealed a cloud point temperature (T_{CP}) of 32.7 °C (Figure S3, Supporting Information). As a result, the modified polymer remains water-soluble at room temperature, allowing the green electrospinning into nanofibers.[80]

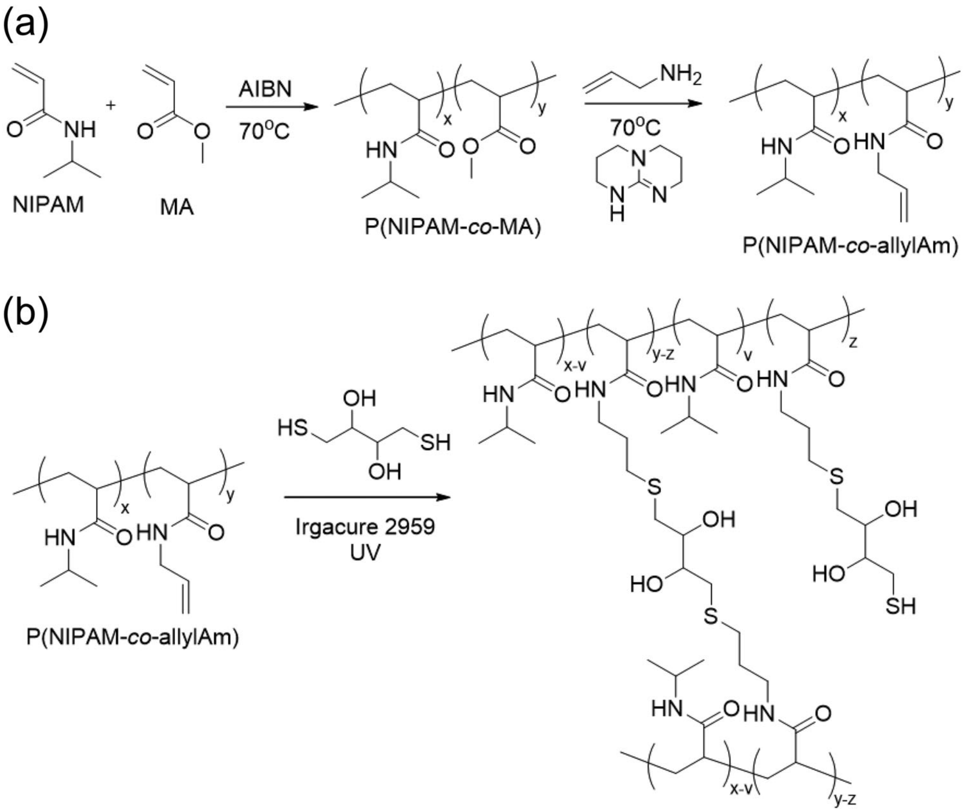

Figure 4. a) Copolymerization of NIPAM with MA followed by amidation with allyamine to form P(NIPAM-*co*-AllylAm), enabling b) photo-crosslinking with dithiothreitol to form a water-insoluble polymer network.

2.3. Electrospinning, Crosslinking, and Functionalization of PNIPAM

The P(NIPAM-*co*-AllylAm) polymer was dissolved in ethanol in the presence of dithiothreitol (DTT) and the photoinitator Irgacure 2959 to form a 20 wt% polymer solution, denoted as the PNIPAM-X solution. The solution was electrospun into a homogeneous nanofibrous mat with fibers having an average diameter of 280 ± 89 nm, followed by UV treatment, which initiated the thiol-ene reaction (Figure 4b). DSC measurements showed that the glass transition temperature (T_g) of the nanofibers after crosslinking increased from 129 to 138 °C, thereby indicating lower chain segment mobility as expected upon successful crosslinking (Figure S4, Supporting Information).

The dimensional stability of the PNIPAM-X nanofibers at the microscale was tested by examining the fibers' microstructure after storage in demineralized water at various temperatures and buffer solutions at pH 4 and 10 for 3 days (**Figure** 5a–e). In all cases, the fibers swelled but maintained their fibrous structure, ensuring the material's integrity. Additionally, the nonwoven was exposed to a salt solution simulating human sweat (Figure 5f). Human sweat mainly consists of water and electrolytes, with sodium chloride (NaCl) being the most prominent salt at an average concentration of 50 mmol L^{-1}. After 3 days of immersion in the salt solution, no changes in the microstructure were observed compared to storage at the same temperature in demineralized water.

Water contact angle (WCA) measurements of both the non-crosslinked and crosslinked nonwovens revealed complete wetting within milliseconds (thus a WCA of 0°), making them both superhydrophilic. However, compared to conventional PNIPAM nanofibers that dissolve immediately upon contact with water, the PNIPAM-X nonwoven exhibits high water stability, significantly expanding its application field, for example, toward dedicated skin-contact smart textile applications.

A conductive and biocompatible silver (Ag) nanoparticle layer was deposited on the PNIPAM-X nanofibrous membranes using physical vapor deposition (PVD). This resulted in a 50 nm-thick silver layer that did not visibly alter the membrane's microstructure. Given the relative surface roughness of nanofibers compared to a flat surface and the fact that PVD is a surface technique, slight variations in thickness, especially in the sample depth, can occur. However, no macroscopic visual changes are observed after the PVD process, and the electrical conductivity of the Ag-coated PNIPAM-X remains uniform over a 10 cm^2 sample. Additionally, the Ag layer has a high water stability while maintaining the membrane's flexibility, ensuring the material's comfort is not compromised. This water stability was demonstrated by measuring the washing water after 5 consecutive pore-opening cycles (at 40 °C and 85% RH) and after washing cycles (in water <10 °C) using UV–vis spectrophotometry (see Figure S5, Supporting Information). This indicates that there is only marginal Ag leaching, especially compared to a reference solution containing 0.02 mg mL^{-1} Ag nanoparticles of 10 nm in an

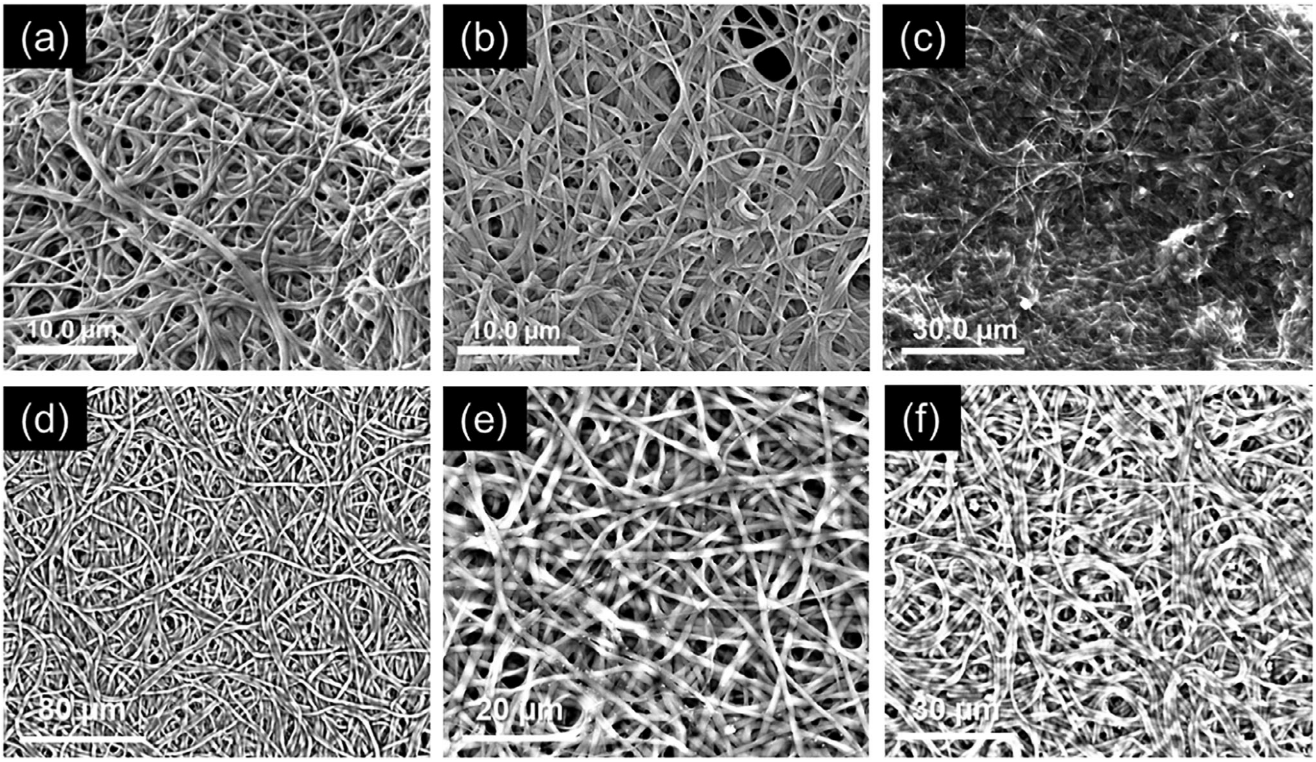

Figure 5. SEM images of PNIPAM-X samples after immersion for 3 days in demineralized water at a) 6 °C, b) 22 °C, and c) 50 °C; buffer solutions at 22 °C of d) pH 4, and e) pH 10; and f) 50 mmol L^{-1} NaCl solution at 22 °C as a simulation of human sweat.

aqueous buffer, which already shows a clear absorbance between 350 and 600 nm even at this low concentration. It has previously been shown that PVD can deposit wear-resistant coatings using, among other materials, nitrides or carbides.[81–85] However, Ag is a relatively ductile material, making it prone to wear over multiple cycles. To increase the hardness of the Ag layer, alloying with, e.g., Cu or Pd has previously been demonstrated to improve wear, thereby likely enhancing the washability of the DEST.[86–88]

2.4. Humidity-Driven Thermoresponsiveness of PNIPAM-X Nanofibers

Given the thermosensitive nature of PNIPAM, which persists after the functionalization and crosslinking of the modified P(NIPAM-*co*-AllylAm), the thermoresponsivity of the electrospun PNIPAM-X nonwovens was studied. For this, 3-legged triangle-shaped cuts, as depicted in Figure 3b, were cut into the electrospun nonwoven. This nonwoven was spun on an aluminum collector with a honeycomb pattern, resulting in fiber-dense zones at the honeycomb bars (Figure 3a). This allows for zones that provide mechanical rigidity and zones that more easily extract and contract in response to temperature or humidity. Combined with the macroscopic cutting pattern, this creates macropores that open when RH and/or temperature increase (**Figure** 6a). Immersion in water enables the pores to recover, closing ≈85% (Figure 6b, left). When reintroduced to a high-humidity environment, the pores reopen (Figure 6b, right). In addition, there is no visual out-of-plane displacement of the nonwoven upon opening and closing the pores, as shown in the side view images of Figure 6. This results in a zero Poisson nonwoven layer without overall tension throughout the material when fully covered by the cutting pattern, due to the material's thermoresponsiveness rather than external mechanical forces. As a result of the dedicated electrospin collector, the mechanically rigid hexagons, with a localized higher fiber density and therefore visible under wet conditions to the human eye, provide overall dimensional stability after multiple opening-and-closing cycles, as demonstrated in Figure S6 (Supporting Information) by outlining several hexagonal honeycomb structures with the same size and under the same angle as the electrospinning collector atop a digital microscope image.

To quantify the pore opening and closing, the honeycomb PNIPAM-X was exposed to different surrounding temperatures at varying relative humidities for 72 h and vice versa (**Figure** 7a,b), as well as immersed in temperature-controlled demineralized water for 24 h (Figure 7c). The surface area covered with nanofibers was determined for a given RH and temperature by pixel analysis of top-view images using ImageJ (**Figure** 8a). The lower the surface area, the larger the honeycomb macropores of the nonwoven. In all cases, the macropores induced by the honeycomb pattern increase in size as the temperature rises (Figure 7a) or the RH increases (Figure 7b), until they are fully opened by local shrinkage of the nonwoven material, bringing the fibers closer together. As demonstrated in Figure 6, there is almost no out-of-plane displacement of the sample as a result of this contraction, especially when compared to the first proof-of-principle samples with cross-shaped cuts in

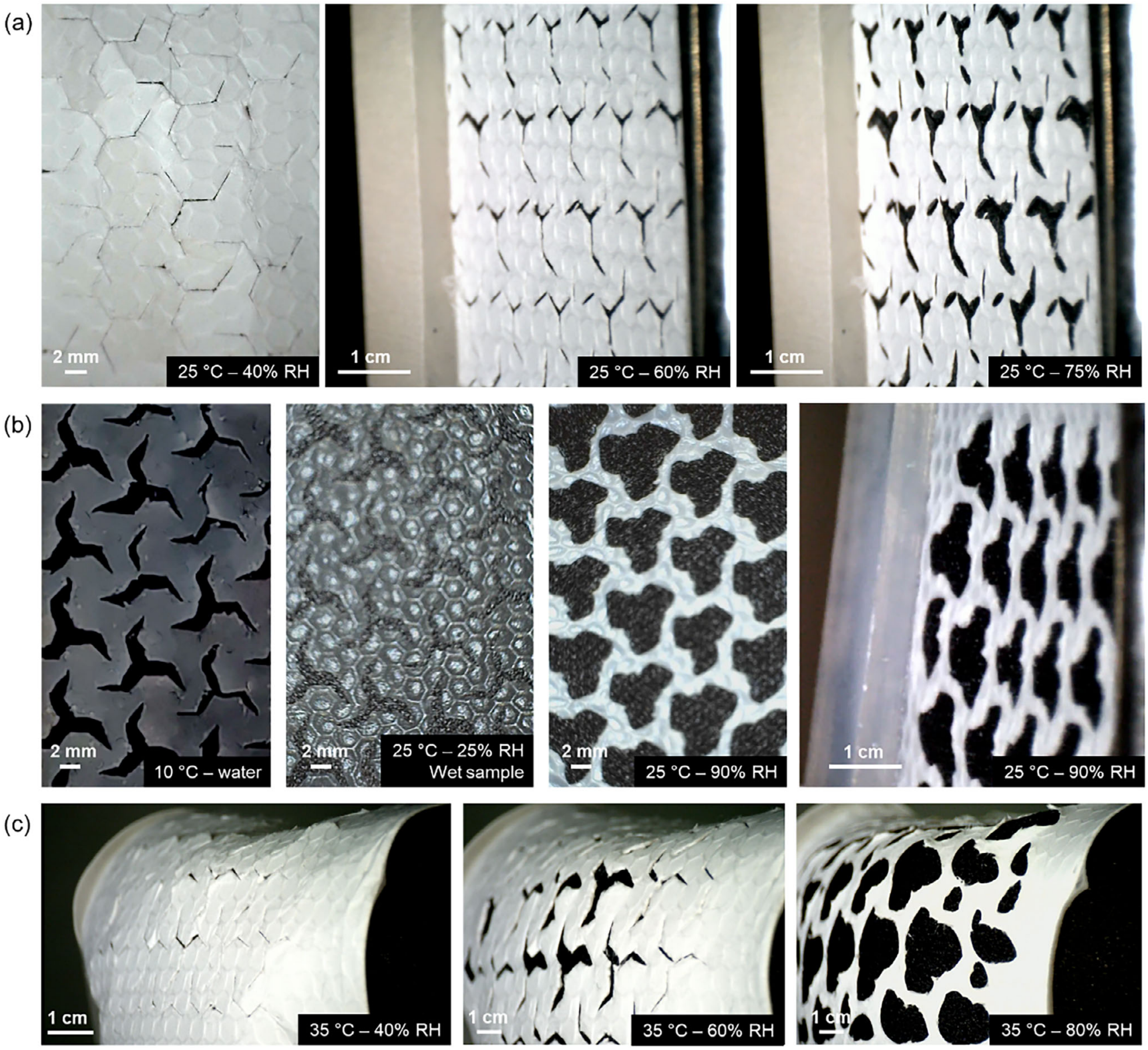

Figure 6. Macroscopic stability of honeycomb PNIPAM-X layer a) upon increasing the RH from 40% to 75% at 25 °C, followed by b) immersion in cold water (10 °C), and reintroduction in an increasingly humid atmosphere at 25 °C. c) Macroscopic stability of a pre-curved DEST upon increasing the RH from 40% to 80% at 35 °C.

electrospun nonwoven (Figure 8b). The combination of our dedicated spinning collector and cutting pattern, therefore, results in a nanofibrous metamaterial layer that maintains dimensional stability during pore opening and closing. The higher the relative humidity or temperature, the sooner we see the pore-opening process. Once a threshold combination of RH and temperature is reached, thermoresponsiveness, and thus pore opening, occurs quite rapidly. This is demonstrated by placing a sample in a climate chamber at 35 °C and 90% RH after storage at 23 °C and 25% RH, resulting in complete pore opening within less than 4 min (Figure 7d).

Upon immersion in water, the pores always open slightly, even at temperatures as low as 6 °C, with an opening of ≈20% of the initially covered surface area (Figure 7c). An increase in water temperature linearly decreases the surface area covered by nanofibers. Furthermore, this process is entirely reversible. The gradual cooling of water from 50 to 10 °C leads to a corresponding gradual reduction in pore size. Given the initial 20% loss of fiber coverage, the opening and closing of pores in water are entirely reversible. Pores that open under high humidity need to be submerged in water to close again. The locally contracted nanofibers do not unwind when cooled, but immersing them in water restores the closed state. Indeed, upon immersion of the opened structure in cold water (< 15 °C), the surface area covered with nanofibers can be increased again to 80% of the initial (closed) sample size, similar to the water-stored samples (Figure 6c). This

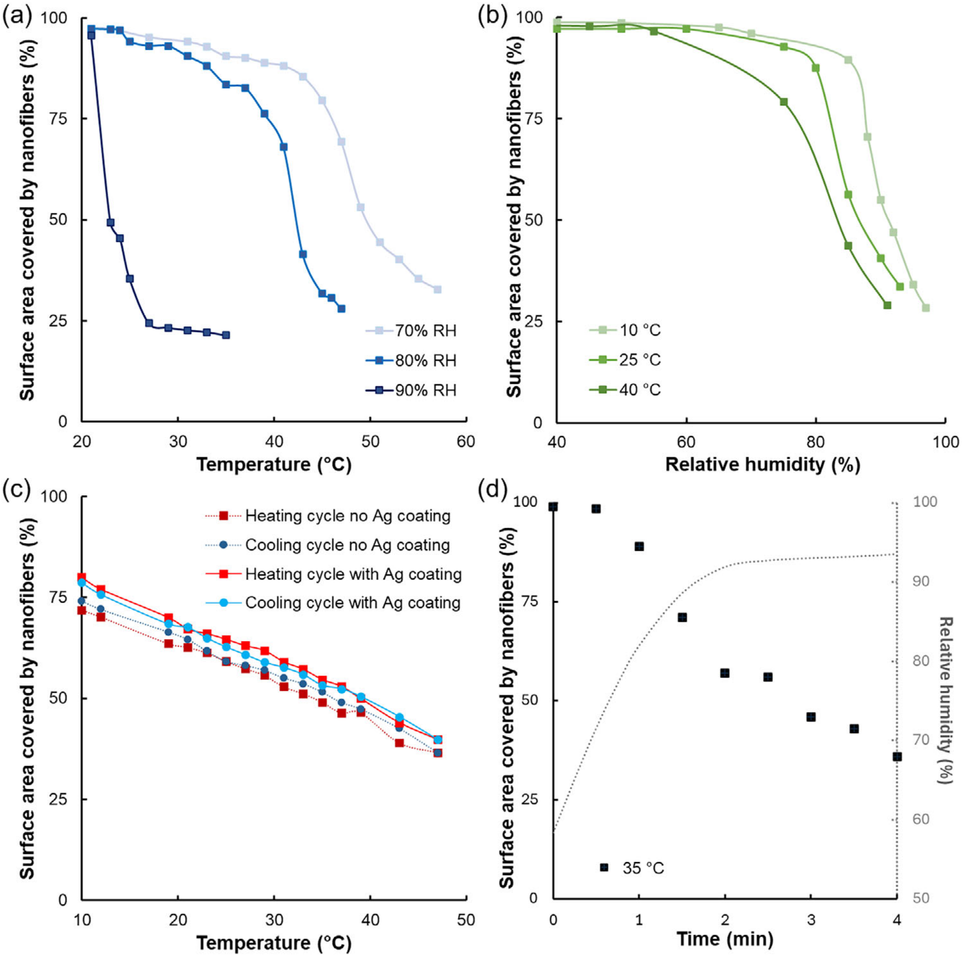

Figure 7. Thermosensitivity of the PNIPAM-X nanofibers upon varying temperature by tracking the surface area covered by nanofibers at a) different RH and b) different ambient temperatures while keeping the other parameter constant; as well as c) immersion in water at varying temperatures. d) Time scale of thermoresponsiveness assessed by measuring nanofiber coverage under sudden climate change to 35 °C and 90% RH (initial climate: 23 °C, 25% RH).

effect is not hindered by the Ag PVD coating (Figure 7c), making it an ideal candidate for use as a nonwoven layer on top of high-emissivity textiles, as discussed in the final section.

2.5. Electromagnetic and Thermal Properties

To demonstrate the potential of our passive, dual-mode thermoregulating electrospun Ag-coated modified PNIPAM-X nonwoven layer, we investigated the electromagnetic properties of the sealed DEST with a honeycomb pattern. This was done both with and without the Ag coating by irradiating the sample with light of different wavelengths relevant for thermal regulation of human bodies. This allowed measuring the reflectance and transmission, and calculating the absorbance, considering that the total equals 100% (**Figure 9**).

Without applying the Ag coating, the PNIPAM-X nonwoven exhibits a very high transmission rate combined with a very low reflectance across the entire wavelength range investigated. If the light is not transmitted through the sample, it is absorbed by the sample (Figure 9a). This is mainly relevant for light with a wavelength ≈6 µm, where a steep drop in transmission is observed. Given that this light falls within the mid-IR range, it will locally heat the material.

Applying the Ag coating on the nanofibers significantly increased the reflectivity across the entire wavelength range, while also reducing the transmission (Figure 9b). This creates the potential to reflect incoming heat away from the fabric to the environment, a requirement for an efficient DEST.

Next, the electrospun Ag-coated PNIPAM-X nonwoven layer was applied to a unidirectional carbon fiber fabric to visually demonstrate the thermal properties and thus the potential for passive thermal regulation. Both the temperature profiles of the top layer of the fabric in its closed/reflection and open/emission modes were measured using an IR camera while varying the temperature underneath the fabric (**Figure 10**).

In its closed mode, the sample without an Ag coating is significantly warmer than the Ag-coated sample, both at low and high temperatures (Figure 10a). Without the Ag coating, the heat from underneath the fabric is transferred to the environment due

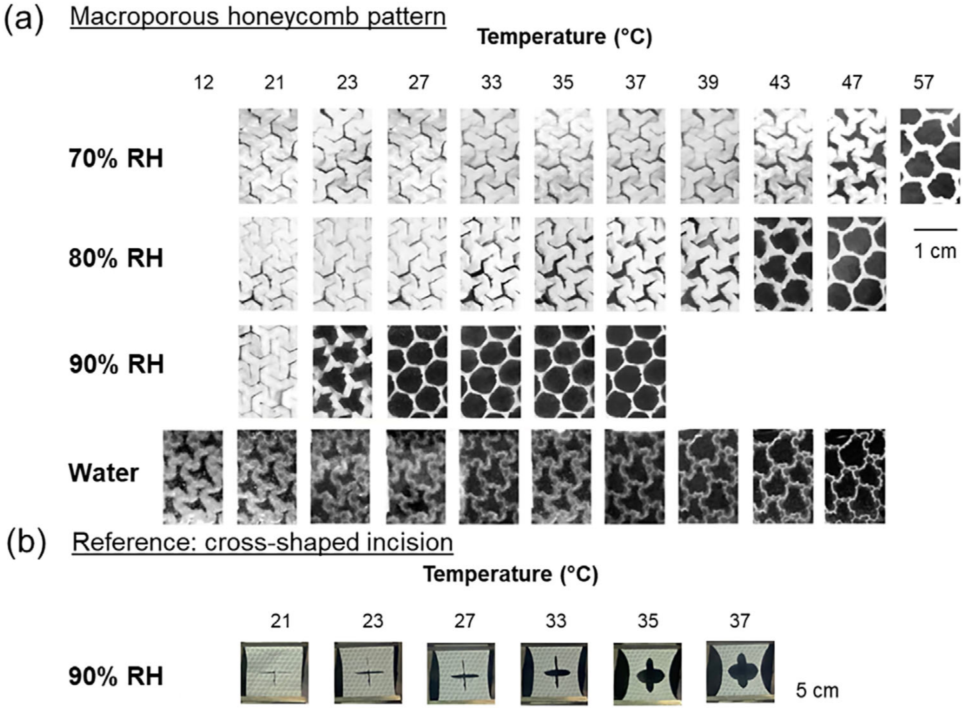

Figure 8. Digital microscopy images illustrating the impact of incorporating a) the macroporous honeycomb cutting pattern on the overall stability of the nanofibrous top layer when exposed to various thermal conditions under high relative humidity or immersion in water, compared to b) a reference sample with a simple cross-shaped cut at 90% RH.

to extensive transmission and absorption of the IR light in the nonwoven layer, leading to heat loss from the body below. Upon incorporation of the Ag PVD layer, the body heat is reflected back to the thermally radiating body, hindering the temperature loss to the surrounding ambient environment. The proposed DEST thus allows maintaining the heat below the fabric when the honeycomb macropores are closed.

When looking at a fabric with an open honeycomb structure (thus, large macropores of the electrospun nonwoven), both fabrics allow similar dissipation of heat to the surrounding environment (Figure 10b). Above a certain threshold temperature, which is lower at a higher relative humidity (Figure 7a), the pores of the DEST open, allowing the built-up body heat to be dissipated to the environment.

2.6. Application Design Rationale

With the large reflection rate of the fabric, as well as the pore opening and closing mechanism now established, the application potential of the proposed DEST is highlighted through a case study of a sports T-shirt designed to regulate a person's temperature while they are sweating, focusing on the dry-to-humid regime. Initially, the honeycomb pores are closed, allowing the person to keep their body heat. Upon engaging in physical activity, one will begin to get warm and sweat, a natural mechanism for regulating body temperature. This will increase the relative humidity underneath the T-shirt. As a result of this increase in temperature and relative humidity, the honeycomb pores will start to open up, allowing heat and moisture dissipation to the surrounding environment, as schematically depicted in Figure 1. Given the honeycomb pattern, the dimensional stability of the nonwoven layer is ensured without significant out-of-plane nonwoven disposition (Figure 6). Upon contact with cold water, the honeycomb pores close again by 85%, after which the opening-and-closing process is reusable.

A more detailed view of the emissivity of our DEST (both experimentally and modeled) for body-contact applications is presented in **Figure 11a**, where it is plotted over the human body emissivity reported in the literature at a skin temperature of 34 °C and a standard human body emissivity of 0.99.[89] The designed DEST has an overall emissivity ϵ_{eff} of ≈0.3 when integrated over the wavelengths of interest for thermal regulation of human body emission (5–20 µm). This experimentally established emissivity was compared to the simulated emissivity for an electrospun nonwoven with a nanofiber diameter of 200 nm, a thickness of 150 µm, and a coverage factor (C_f) of 0.85. This shows a relatively good prediction of the effective emissivity using this electromagnetic model. Upon varying the fiber diameter and fabric thickness in the electromagnetic model, an ϵ_{eff} as low as 0.2 can be achieved. There is, however, a slight visible discrepancy in the absorption/emission spectrum at lower wavelengths between the experimental data and the simulation. This is probably due to the absorption of 6–7 µm radiation by PNIPAM-X nanofibers that are not fully coated and are seated deep in the membrane volume.

Based on the experimentally established thermoresponsive behavior of the nonwoven material with a honeycomb pattern cut, as shown in Figure 8, the C_f can range from 1 for the initial closed DEST to nearly zero when all the honeycomb pores are maximally open. In practice, values between 0.25 and 0.85 are

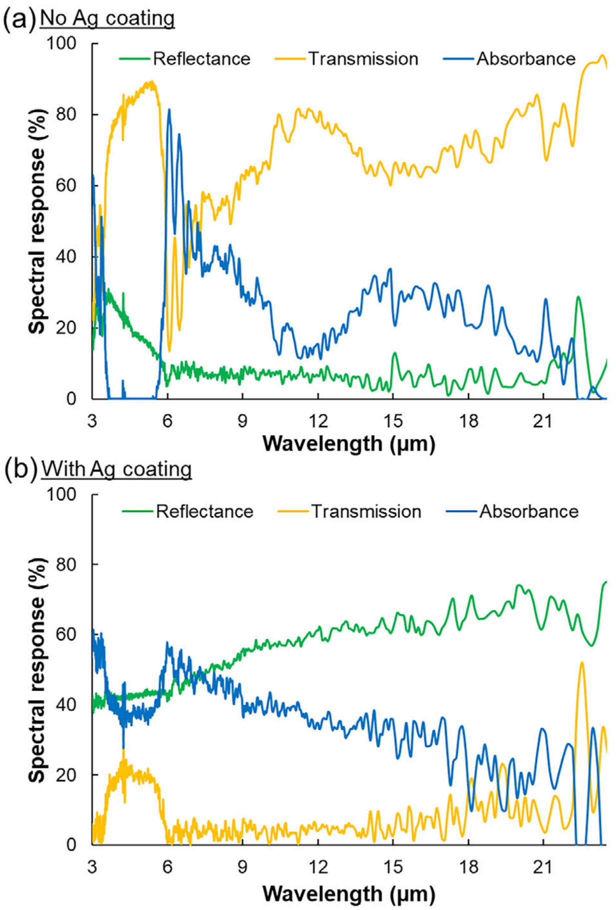

Figure 9. Infrared reflection, transmission, and absorption spectra of honeycomb pattern cut PNIPAM-X nanofibrous membranes, a) without Ag coating and b) with Ag coating, showing a significant increase in reflectance upon introducing the Ag layer on top of the DEST.

achieved (Figure 7a–c), resulting in the subsequent highest and lowest setpoints of 25 and 19 °C, respectively, based on Equations S7–S21 (Supporting Information) described in Section S1 (Supporting Information) (Figure 11b). When comparing these setpoints (green arrow) to the ideal scenario (purple arrow), where C_f can vary from zero to one, and the modeled scenario (dark red arrow), the setpoint window is lower. A thermal comfort window of 6 °C can be achieved, which is a significant improvement over a conventional sport T-shirt, making our honeycomb pattern electrospun nonwoven an ideal candidate for further exploration of thermoregulating skin-contact applications.

In addition to the thermo- and humidity-responsive nature of our DEST, it is known that the presence of anions also influences the LCST of PNIPAM.[90–93] The Hofmeister series provides a qualitative hierarchy of anions based on their capacity to precipitate proteins in aqueous solutions.[94–96] It includes several common anions found in human sweat relevant for this case study, such as chloride (Cl^-), bicarbonate (HCO_3^-), phosphate ($H_2PO_4^-$ or HPO_4^{2-}), and sulfate (SO_4^{2-}). Upon using a T-shirt made from our proposed DEST, interactions with these anions will likely influence the thermoresponsive behavior. This has already been demonstrated for microgels[91] and hydrogel sponges.[93] This is promising for future work on our PNIPAM-X electrospun nonwoven. It was even demonstrated that altering the molecular weight of the PNIPAM in solution increases the tunability of this effect. This could enable our PNIPAM-X material to be used in various climates, such as developing clothes for areas with high RH and temperature during summer, where wearers transition from air-conditioned rooms with low RH and temperature to high RH and temperature outside.[90]

3. Conclusion

A multilayered dynamic IR emissivity-modulating material was designed and fabricated to provide passive thermoregulation. By combining layers with different emissivity values with a top layer that undergoes thermally induced expansion and contraction, a surface with tunable and programmable effective emissivity is achieved. This highlights the high potential for developing thermoregulating textiles. Although this is a simple principle, different material selection and design aspects must be considered to ensure overall dimensional stability, enable environmentally friendly production, and ideally, make it biocompatible for skin-contact applications.

In this work, a modified crosslinked PNIPAM nanofibrous nonwoven coated with Ag was developed as such a thermoresponsive top layer. Using an electrospun nonwoven instead of a traditional textile creates a significantly higher specific surface area due to its small fiber diameter, resulting in greater shape-changing potential. As a result of the LCST of PNIPAM, which is ≈32 °C, thermal expansion/contraction is achieved around this temperature. It is observed that the response temperature decreases when the surrounding relative humidity increases or when the structure is immersed in water, resulting in a faster contraction of the structure. After humidity- and/or temperature-induced contraction of the nonwoven, immersion in cold water (< 10 °C) allows the sample to restore up to 85% of its original size. This volume loss upon recovery is no longer observed after this initial cycle.

To create an overall dimensionally stable top layer, an in-house developed cutting pattern was incorporated into the nonwoven after electrospinning on a dedicated honeycomb-structured collector. As a result, honeycomb-shaped macropores are opened or closed by the humidity- and temperature-induced contraction and expansion of the structure. Together with the Ag coating, this creates a dimensionally stable metamaterial with passive emission and reflection modes.

The potential of our honeycomb-pattern nonwoven top layer was demonstrated through a proof-of-concept application on a unidirectional carbon fabric in a dry-to-humid regime. This shows the thermal comfort potential of the layer at ≈6 °C. This represents a significant improvement over conventional textiles, which lack a thermal comfort range, making great strides toward the development of clothing for thermal management control in dedicated climates around the world.

4. Experimental Section

Materials: All chemicals were used as received unless otherwise stated. Neutral Al_2O_3 was purchased from Fischer Scientific,

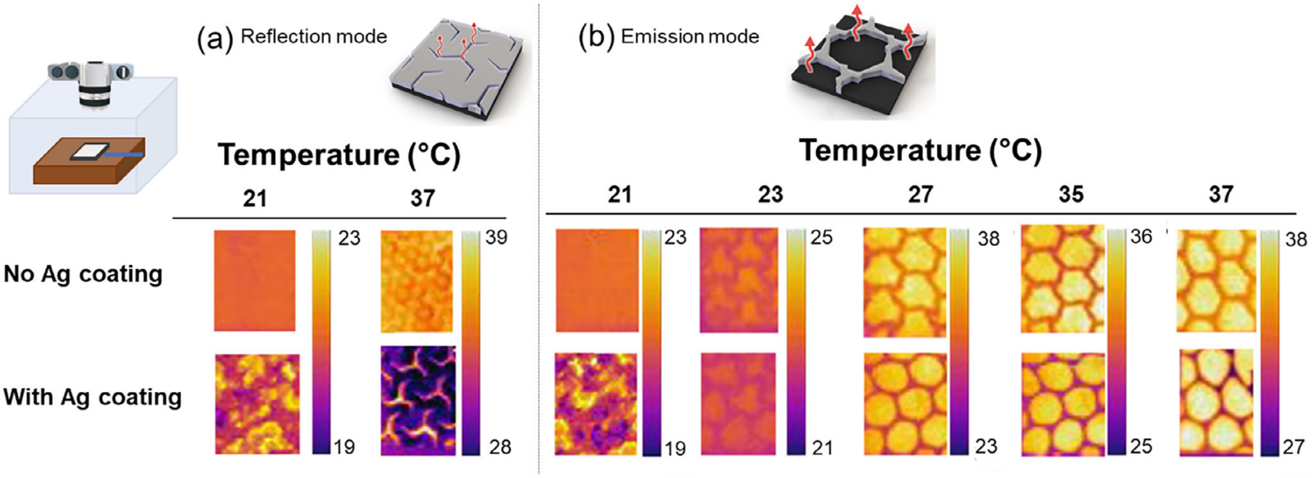

Figure 10. IR camera image of the nanofibrous Ag-coated DEST with the honeycomb pattern cut at different temperatures of a heating block underneath the sample at 85% RH in a) heating/closed and b) cooling/open mode, showing the working principle of the heat storage or transfer with changing conditions. For every sample, the measured temperature profile of the IR camera is given on the right of the pictures. In its closed state, there is a limited temperature loss of the DEST to the ambient environment.

N,N-dimethylacetamide (DMA, ≥99%), N,N-dimethylformamide (DMF, ≥99%), diethylether (Et_2O, >99%), triazabicyclodecene (TBD, 98%), allylamine (99%), methylacrylate (99%), and N-isopropylacrylamide (NIPAM, 97%) were purchased from Sigma–Aldrich. BASF kindly donated Irgacure 2959. 2,2′-Azobis(2-methylpropionitrile) (AIBN) was purchased from Sigma–Aldrich and recrystallized from methanol before use. Deuterated chloroform ($CDCl_3$) was purchased from Eurisotop. Colloidal silver solution (4000 ppm) was purchased from Argenol.

Synthesis of P(NIPAM-co-MA): P(NIPAM-*co*-MA) was synthesized via free radical polymerization, using AIBN as the initiator. In detail, 10 g of NIPAM (420 equiv, 0088 mol), 3.4 mL of DMA (180 equiv, 0.038 mol), 40 mL of DMF, and 34 mg of AIBN (1 equiv, 0.21 mmol) were combined in a 100 mL round-bottom flask. Next, the flask was cooled in an ice bath and degassed by bubbling argon through the reaction mixture for 1 h. Next, the polymerization was performed at 70 °C, and the reaction progress was monitored online using GC. The polymerization was continued until full conversion, and the polymer was isolated as a white powder by precipitation in cold diethyl ether.

A Bruker Avance 300 MHz Ultrashield was used to measure ^{1}H-nuclear magnetic resonance (^{1}H NMR) spectra at room temperature. The chemical shifts are given in parts per million (δ) relative to tetramethylsilane, and chloroform-d was used as solvent.

Size-exclusion chromatography (SEC) was performed on an Agilent 1260-series HPLC system equipped with a 1260 online degasser, a 1260 ISO-pump, a 1260 automatic liquid sampler (ALS), a thermostatted column compartment (TCC) set at 50 °C equipped with two PLgel 5 µm mixed-D columns (7.5 mm × 300 mm) and a precolumn in series, a 1260 diode array detector (DAD) and a 1260 refractive index detector (RID). The used eluent was DMA containing 50 mM of LiCl at a flow rate of 0.500 mL min^{-1}. The spectra were analyzed using the Agilent Chemstation software with the GPC add-on. Molar mass values and molar mass distribution, i.e., dispersity (Đ) values, were calculated against poly(methyl methacrylate) standards from PSS.

Gas chromatography (GC) was performed on an Agilent 7890A system equipped with a VWR Carrier-160 hydrogen generator and an Agilent HP-5 column of 30 m length and 0.320 mm diameter. A flame ionization detector was used, and the inlet was set to 250 °C with a split injection ratio of 25:1. Hydrogen was used as carrier gas at a flow rate of 2 mL min^{-1}. The oven temperature was increased by 20 °C min^{-1} from 50 to 120 °C, followed by a ramp of 50 °C min^{-1} to 300 °C.

Infrared (IR) spectra were measured on a Perkin-Elmer 1600 series FTIR spectrometer and are reported in wavenumber (cm^{-1}). Lyophilisation was performed on a Martin Christ freeze-dryer, model Alpha 2-4 LSC plus.

Following properties of the synthesized polymer were obtained: DMA-SEC: Mn = 32.4 kDa, Đ= 3.97; ^{1}H NMR (300 MHz, Chloroform-d) δ 7.11–5.69 (m, 2H), 4.03 (m, 2H), 3.66 (m, 3H), 2.56 (m, 1H), 2.46–1.26 (m, 9H), 1.17 (m, 12H). MA content = signal 3.66 ppm/(signal 3.66 ppm + (signal 1.17 ppm/2)) = 3/9= 33% MA.

Synthesis of P(NIPAM-co-allylAm): A total of 10 g of P(NIPAM-*co*-MA) (32.7 mmol of MA groups, 1 equivalent of MA groups), and TBD (714 mg, 5.1 mmol, 0.16 eq.) were dissolved in 51 mL of allylamine (670 mmol, 20 eq) in a 100 mL round-bottom flask equipped with a stir bar. The reaction mixture was degassed by bubbling argon through the solution for 30 min. Subsequently, the reaction mixture was heated to 70 °C and left to react for 3 days. Next, allylamine was evaporated using a rotary evaporator, and the polymer was dissolved in DCM and precipitated in excess diethyl ether (500 mL). The precipitate was dried overnight in the vacuum oven. Subsequently, the polymer was dissolved in water, and a small amount of Dowex 50WX8 was added, followed by stirring overnight. Next, the Dowex was filtered off, and the solution was frozen in liquid nitrogen and freeze-dried. SEC: Mn = 45.8 kDa, Đ= 3.83; ^{1}H NMR (300 MHz, chloroform-d, δ): δ 7.19 (m, 3.3H), 5.74 (m, 1H), 5.07 (m, 1.8H), 3.84 (m, 3.7H), 2.91–1.17 (m, 11.7H), 1.07 (m, 10.2H).

The cloud point temperature of the polymer solutions was determined using turbidimetry on an Avantium Crystal 16 turbidimeter. A 1 mL sample of 10 mg mL^{-1} was examined by cycling the temperature between 10 and 80 °C, and the T_{CP} was determined as the temperature at which the transmission had decreased to 50% during heating. The heating rate was set at 0.5 °C min^{-1}.

Electrospinning: Poly(NIPAM-*co*-AllylAm) (0.6 g), DTT (30 mg), and Irgacure D-2959 (5 mg) as the photoinitiator were dissolved in ethanol (3 mL) to form a 20 wt% solution. The solution was stirred at room temperature for 6 h in UV-insulating vials to prevent pre-crosslinking. Otherwise, crosslinks in the spinning solution would increase the dynamic viscosity to an extent that would hinder the electrospinning process. The nanofibers were electrospun with a flow rate of 0.75–1.5 mL h^{-1}, a tip-to-collector distance of 12–15 cm, and an applied voltage of 15 kV. An in-house printed aluminum collector with a thickness of 2 mm and honeycomb-shaped holes was used to collect the electrospun nonwoven (details see Figure 3), till a thickness of 82 ± 17 µm was reached. The obtained nanofibers were placed under a 300 W Osram Ultra-Vitalux UV lamp (mainly UV-A with

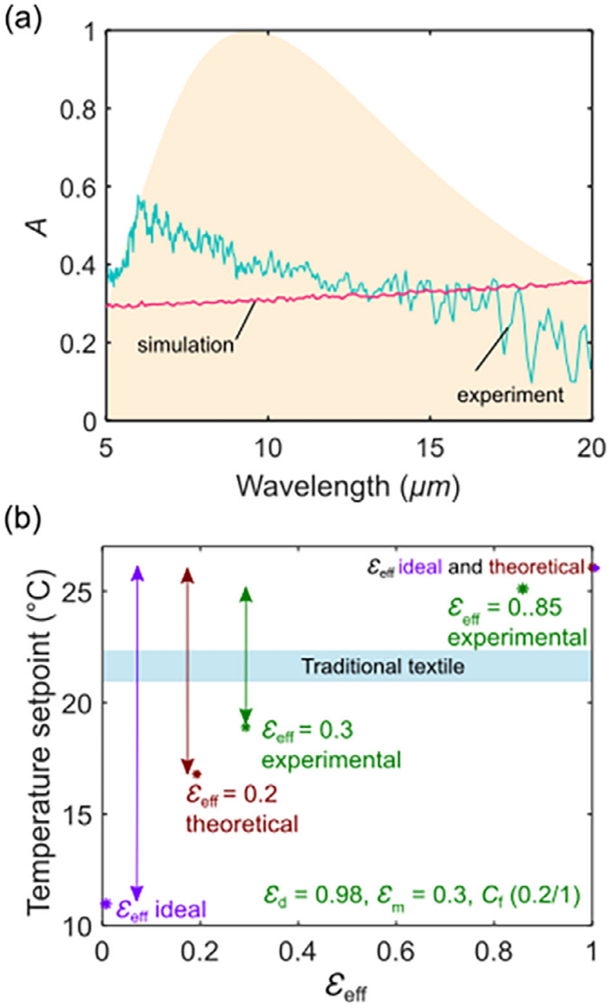

Figure 11. a) Measured and simulated absorption spectra of Ag-coated nanofibrous DEST plotted over the human body emissivity at standard human body conditions of 34 °C skin temperature and emissivity of 0.99. b) Temperature setpoint range as a function of the effective emissivity of the Ag-coated nanofibrous DEST compared to a classical textile, the theoretical and ideal effective emissivity aimed for in DESTs.

intensity of ≈5 mW cm^{-2}) at a distance of 10 cm for 1 h on both sides of the nonwoven. Details associated with preliminary optimization of this production process can be found in Section S2 (Supporting Information).

Functionalization of Crosslinked PNIPAM: Silver (Ag) deposition on the crosslinked P(NIPAM-*co*-AllylAm) nanofibers, denoted as PNIPAM-X, was performed using physical vapor deposition (PVD) in an in-line stainless-steel chamber via magnetron sputtering (DISCOVERY-365, Denton). The deposition chamber was evacuated to an ultimate pressure of 1.10^{-7} Torr. The system was equipped with a plate magnetron cathode. A rectangular silver target (300 mm × 50 mm) was sputtered in pure Ar gas at a flow of 70 sccm. The substrate was placed on the conveyor, carried back and forth under the cathode. The target was sputtered in the DC mode at a power of 500 W (3.3 W cm^{-2}). The working pressure during the deposition was fixed at 3 mTorr. Prior to Ag deposition, the PNIPAM-X surface was ion-cleaned to remove residual contaminants and activate it, thereby promoting strong adhesion between the metal layer and the substrate. A 50 nm Ag film was deposited under a 3 mTorr Ar sweep to minimize oxidation during deposition.

Characterization of Nanofibrous Membranes: Scanning Electron Microscope (SEM) analyses were performed using a FEI Quanta 200 F SEM with an acceleration voltage of 20 kV. Before SEM analysis, the samples were coated with a thin layer of gold via a sputter coater (Emitech SC7620). The nanofiber diameters were measured using ImageJ software by taking an average of 50 measurements per sample.

The Fourier Transform Infrared Spectroscopy (FTIR) spectra were recorded using a Nicolet iS50 FTIR setup with OMNIC software in the range 400–4000 cm^{-1} with a resolution of 4 cm^{-1} and 32 scans for each measurement.

Modulated temperature differential scanning calorimetry (DSC) traces were analyzed using a TA Instruments Q2000, equipped with a refrigerated cooling system (RCS90) and a nitrogen purge gas (50 mL min^{-1}). The instrument was calibrated using T_{zero} technology with standard T_{zero} aluminum pans, utilizing indium at the heating rate employed during the measurement. The heating rate was set at 2 °C min^{-1}, and samples of 2.5 ± 0.5 mg were used. The selected temperature modulation was ± 0.5 °C every 40 s. The samples were analyzed through two heating cycles, during which they were heated from 0 to 250 °C.

Water-stability tests were performed both before and after crosslinking. Therefore, the nanofibers were immersed in deionized water at different temperatures, and their dimensional stability was subsequently measured. Water contact measurements were performed with a 5 μL deionized water droplet on a DSA 30 Krüss GmbH drop shape instrument at room temperature. For each sample, 10 measurements were taken to obtain reproducible results.

The visual inspection of the opening and closing of the DEST was followed using a Dino Lite Premier Digital Microscope, with the samples clamped in a sample holder within a Weiss Technik Lab Event 150 climate cabinet at varying temperatures and relative humidities.

The Ag leaching from the DEST after multiple washing cycles was determined by measuring the transmission spectra of the washing water using a Perkin-Elmer Lambda 900 UV–vis spectrophotometer, recording absorbance between 350 and 750 nm, and comparing them to a silver dispersion as a reference solution. This reference was a 10 nm dispersion of 0.02 mg mL^{-1} in an aqueous buffer containing sodium citrate as stabilizer.

The reflectance, transmittance, and absorbance (1-reflectance-transmission) of the samples were characterized using a Shimadzu IR Prestige 21 FTIR spectrometer. The infrared measurements were carried out using an integrating sphere (Mid-IR IntegratIR—PIKE technologies), which features a 12-degree illumination of the sample to measure the total (diffuse and specular) relative reflectance (compared to a standard gold sample). The samples were placed directly onto the sample port (diameter of 2.5 cm), located at the top of the sphere, for reflectance measurements. For the transmittance measurements, the samples were placed in front of the entrance port, and the sample port, located on top of the sphere, was covered with gold reference material.

A FLIR T420 high-performance infrared camera with an onboard visual camera was used to monitor the heat dissipation of the samples during the opening and closing of the honeycomb pores in contact with human skin.

Modeling: With the ambient setpoint temperature as a final result, the electromagnetic and thermal modeling framework is divided into three categories. The emissivity of the top layer was investigated using an electromagnetic model (solving the scattering problem) and a radiative transport model (solving the RTE). Subsequently, the setpoint was calculated with the thermal model (solving the heat balance equation). The initial phase involved applying the conventional Lorenz–Mie solutions for a cylinder to determine the optical properties of an individual metallic nanofiber. This encompassed the efficiencies of scattering $Q_{sca}(\alpha)$, extinction $Q_{ext}(\alpha)$, and absorption $Q_{abs}(\alpha)$, along with the scattering phase function $\Phi(\alpha, \Theta)$. Here, α and Θ designate the incident and scattering angles, respectively. Subsequently, by using the incoherent summation rule, the effective radiative properties of a nanofiber cloud uniformly dispersed in air were calculated (e.g., asymmetry factor g, scattering albedo $\omega_0(\alpha)$, effective absorption $\kappa_{\mathrm{eff}}(\alpha)$, scattering $\sigma_{\mathrm{eff}}(\alpha)$, and extinction $\beta_{\mathrm{eff}}(\alpha)$ coefficients). Using these effective optical parameters, the radiative transfer equation was solved through a collision-based forward Monte Carlo (MC) simulation to retrieve the spectral absorptance and emissivity. Using these spectral results, the total emissivity (integrated over the emission of the human body) of the top layer (ϵ_m) and the effective emissivity of the fabric (ϵ_{eff}) were calculated.

Supporting Information

Supporting Information is available from the Wiley Online Library or from the author.

Acknowledgements

E.L. and M.G.A. contributed equally. The authors acknowledge support from the Interreg V France-Wallonie-Vlaanderen program, under the PHOTONITEX project. K.D.C. thanks the Special Research Fund Ghent University (BOF) for the grant BOF.BAS.2018.0015.01. J.V.G. and R.H. acknowledge the support of the industrial research fund for the grant F2019/IOF-ConcepTT/049. M.G.A. is funded by the Fonds de la Recherche Scientifique-FNRS (Grant No. FC 053809).

Conflict of Interest

The authors declare that they have no known competing financial interests or personal relationships that could have appeared to influence the work reported in this paper.

Data Availability Statement

The data that support the findings of this study are available from the corresponding author upon reasonable request.

Keywords

electrospinning, emissivity, metamaterial design, shape-memory polymer, thermoregulation

Received: September 2, 2025
Revised: November 6, 2025
Published online:

---

[1] J. Chai, J. Fan, *Mater. Today Energy* **2022**, *24*, 100925.
[2] S. Houssainy, L. Taylor, P. Torcellini, S. Ramaraj, *Decarbonizing Building Thermal Systems: A How-to Guide for Heat Pump Systems and Beyond*, Golden, CO: National Renewable Energy Laboratory, OSTI.GOV, **2024**.
[3] R. Talami, I. Dawoodjee, A. Ghahramani, *Buildings* **2023**, *13*, 2998.
[4] K. Huang, H. Lan, S. Li, R. Tan, Y. Si, L. Lei, K. Wang, X. Xu, W. Fang, X. Liang, W. J. Li, J. Hu, *Prog. Mater. Sci.* **2025**, *154*, 101504.
[5] L. Lei, S. Shi, D. Wang, S. Meng, J. G. Dai, S. Fu, J. Hu, *ACS Nano* **2023**, *17*, 1803.
[6] F. L. Zhu, Q. Q. Feng, *Int. J. Therm. Sci.* **2021**, *165*, 106899.
[7] S. Dou, H. Xu, J. Zhao, K. Zhang, N. Li, Y. Lin, L. Pan, Y. Li, *Adv. Mater.* **2021**, *33*, 2000697.
[8] H. Wei, J. Gu, F. Ren, L. Zhang, G. Xu, B. Wang, S. Song, J. Zhao, S. Dou, Y. Li, *Small* **2021**, *17*, 2100446.
[9] Y. C. Zhao, F. Fang, *Surfaces and Interfaces* **2024**, *45*, 103832.
[10] P. Tao, W. Shang, C. Song, Q. Shen, F. Zhang, Z. Luo, N. Yi, D. Zhang, T. Deng, *Adv. Mater.* **2015**, *27*, 428.
[11] S. Dou, H. Xu, J. Zhao, K. Zhang, N. Li, Y. Lin, L. Pan, Y. Li, *Adv. Mater.* **2021**, *33*, 2000697.
[12] X. Li, W. Guo, P. C. Hsu, *Adv. Mater.* **2024**, *36*, 2209825.
[13] X. Yu, Y. Li, X. Yin, X. Wang, Y. Han, Y. Si, J. Yu, B. Ding, *ACS Appl. Mater. Interfaces* **2019**, *11*, 39324.
[14] R. Xiao, C. Hou, W. Yang, Y. Su, Y. Li, Q. Zhang, P. Gao, H. Wang, *ACS Appl. Mater. Interfaces* **2019**, *11*, 44673.
[15] M. G. Abebe, E. Khousakoun, H. Gidik, E. Mohsenzadeh, S. Desprez, B. Maes, *ACS Appl. Opt. Mater.* **2024**, *2*, 963.
[16] M. Boutghatin, Y. Pennec, B. Djafari-Rouhani, A. Akjouj, V. Gaucher, H. Gidik, S. Assaf, M. Carette, V. Thomy, *Adv. Mater. Technol.* **2022**, *7*, 2101738.
[17] H. Gidik, G. Bedek, D. Dupont, C. Codau, *Sens Actuators A Phys* **2015**, *230*, 25.
[18] M. G. Garzon Altamirano, M. G. Abebe, J. Lejeune, A. Cayla, B. Maes, J. Odent, J. M. Raquez, C. Campagne, E. Devaux, *J. Appl. Polym. Sci.* **2023**, *140*, 54004.
[19] M. G. Altamirano, M. G. Abebe, N. Hergué, J. Lejeune, A. Cayla, C. Campagne, B. Maes, E. Devaux, J. Odent, J. M. Raquez, *Soft Matter* **2023**, *19*, 2360.
[20] G. A. Muluneh, E. Khousakoun, S. Desprez, J.-M. Raquez, B. Maes, *Proceed. 19th World Text. Conf. -Autex* **2019**, *2019*, 11.
[21] M. G. Abebe, A. De Corte, G. Rosolen, B. Maes, *Phys. Rev. Appl.* **2021**, *16*, 054013.
[22] C. Sun, J. Luo, S. Yan, K. Li, Y. Li, H. Wang, C. Hou, Q. Zhang, C. Sun, J. Luo, S. Yan, K. Li, H. Wang, C. Hou, Y. Li, Q. Zhang, *Adv. Funct. Mater.* **2023**, *33*, 2211035.
[23] Y. Peng, Y. Cui, *Natl. Sci. Rev.* **2024**, *11*, nwae295.
[24] Y. C. Zhao, F. Fang, *Compos. Sci. Technol.* **2023**, *237*, 110013.
[25] X. Zuo, X. Zhang, L. Qu, J. Miao, *Adv. Mater. Technol.* **2023**, *8*, 2201137.
[26] X. Lan, Y. Wang, J. Peng, Y. Si, J. Ren, B. Ding, B. Li, *Mater. Today Phys.* **2021**, *17*, 100342.
[27] Y. Y. Choi, K. Zhou, H. K. Woo, D. Patel, M. Salauddin, L. Cai, *ACS Mater. Lett.* **2024**, *6*, 4624.
[28] E. Pakdel, M. Naebe, L. Sun, X. Wang, *ACS Appl. Mater. Interfaces* **2019**, *11*, 13039.
[29] J. Wang, Q. Li, D. Liu, C. Chen, Z. Chen, J. Hao, Y. Li, J. Zhang, M. Naebe, W. Lei, *Nanoscale* **2018**, *10*, 16868.
[30] M. G. Abebe, G. Rosolen, J. Odent, J. M. Raquez, B. Maes, *Nanoscale* **2022**, *14*, 1421.
[31] X. Zhang, X. Chao, L. Lou, J. Fan, Q. Chen, B. Li, L. Ye, D. Shou, *Compos. Commun.* **2021**, *23*, 100595.
[32] C. Lan, J. Meng, C. Pan, L. Jia, X. Pu, *Mater. Horiz.* **2024**, *11*, 1760.
[33] E. Pakdel, X. Wang, *Mater. Des.* **2023**, *231*, 112006.
[34] W. Deng, C. Shen, P. Wang, G. Zheng, Y. Ji, K. Dai, L. Mi, D. Zhang, C. Liu, C. Shen, *Appl. Surf. Sci.* **2021**, *549*, 149255.
[35] E. Loccufier, D. P. Debecker, D. R. D'hooge, K. De Buysser, K. De Clerck, *ChemCatChem* **2024**, *16*, 202301563.
[36] E. Schoolaert, R. Hoogenboom, K. De Clerck, *Adv. Funct. Mater.* **2017**, *27*, 1702646.
[37] X. Li, Y. Yang, Z. Quan, L. Wang, D. Ji, F. Li, X. Qin, J. Yu, S. Ramakrishna, *Chem. Eng. J.* **2022**, *430*, 133093.
[38] L. C. Hu, C. H. Xue, B. Y. Liu, X. J. Guo, J. H. Wang, F. Q. Deng, *ACS Appl. Polym. Mater* **2022**, *4*, 3343.
[39] A. Liguori, S. Pandini, C. Rinoldi, N. Zaccheroni, F. Pierini, M. L. Focarete, C. Gualandi, *Macromol. Rapid Commun.* **2022**, *43*, 2100694.
[40] A. Xie, L. Zhu, Y. Liang, J. Mao, Y. Liu, S. Chen, *Angew. Chem.* **2022**, *134*, 202208592.
[41] H. Liu, J. Yu, S. Zhang, B. Ding, *Nano Lett.* **2022**, *22*, 9485.
[42] J. Wu, M. Wang, L. Dong, J. Shi, M. Ohyama, Y. Kohsaka, C. Zhu, H. Morikawa, *ACS Nano* **2022**, *16*, 12801.
[43] Z. Yan, H. Zhai, D. Fan, Q. Li, *Nano Today* **2023**, *51*, 101897.
[44] X. Yue, T. Zhang, D. Yang, F. Qiu, G. Wei, H. Zhou, *Nano Energy* **2019**, *63*, 103808.
[45] K. Li, M. Li, C. Lin, G. Liu, Y. Li, B. Huang, *Small* **2023**, *19*, 2206149.

[46] H. Kim, S. McSherry, B. Brown, A. Lenert, *ACS Appl. Mater. Interfaces* **2020**, *12*, 43553.
[47] C. Yang, X. Sun, H. Hu, K. Zhang, Y. Ni, S. Shang, Y. Liu, *Mater. Lett.* **2022**, *320*, 132372.
[48] X. Li, Z. Ding, G. E. Lio, J. Zhao, H. Xu, L. Pattelli, L. Pan, Y. Li, *Chem. Eng. J.* **2023**, *461*, 142095.
[49] H. Baniasadi, M. Madani, J. Seppälä, J. B. Zimmerman, M. R. Yazdani, *J. Energy Storage* **2023**, *68*, 107660.
[50] L. Huang, Y. Chen, Z. Xu, C. He, Y. Li, J. Zhao, Y. Tang, *Nanomaterials* **2023**, *13*, 2313.
[51] J. Wu, M. Wang, L. Dong, C. Zhu, J. Shi, H. Morikawa, *ACS Sustain. Chem. Eng.* **2022**, *10*, 7873.
[52] B. Azimi, L. Thomas, A. Fusco, O. I. Kalaoglu-Altan, P. Basnett, P. Cinelli, K. de Clerck, I. Roy, G. Donnarumma, M. B. Coltelli, S. Danti, A. Lazzeri, *J. Funct. Biomater.* **2020**, 11.
[53] Z. Qin, H. Wang, L. Wang, J. Yao, G. Zhu, B. Guo, J. Militky, D. Kremenakova, M. Zhang, *J. Appl. Polym. Sci.* **2023**, *140*, 54677.
[54] J. Ding, Y. Liu, A. Harsányi, A. Kardos, P. Xavier, R. A. Campbell, I. Varga, *Polymers* **2024**, *16*, 2584.
[55] Q. Shen, C. Fang, L. Hu, M. J. Serpe, *SmartMat* **2024**, *5*, 1254.
[56] P. Skigin, P. Robin, A. Kavand, M. Mensi, S. Gerber-Lemaire, *Polymers (Basel)* **2024**, *16*, 2873.
[57] Y. Liang, J. He, M. Li, Z. Li, J. Wang, J. Li, B. Guo, *ACS Biomater. Sci. Eng.* **2025**, *11*, 1921.
[58] A. Das, A. Babu, S. Chakraborty, J. F. R. Van Guyse, R. Hoogenboom, S. Maji, *Adv. Funct. Mater.* **2024**, *34*, 2402432.
[59] S. Throat, S. Bhattacharya, *Adv. Polym. Technol.* **2024**, *2024*, 1444990.
[60] S. Prylutska, A. Grebinyk, S. Ponomarenko, D. Gövem, V. Chumachenko, N. Kutsevol, M. Petrovsky, U. Ritter, M. Frohme, J. Piosik, Y. Prylutskyy, *Int. J. Mol. Sci.* **2024**, *25*, 3069.
[61] S. Lanzalaco, E. Armelin, *Gels* **2017**, *3*, 36.
[62] A. Das, A. Babu, S. Chakraborty, J. F. R. Van Guyse, R. Hoogenboom, S. Maji, *Adv. Funct. Mater.* **2024**, *34*, 2402432.
[63] D. J. Clarke, F. Carter, I. Jowers, R. J. Moat, *Appl. Mater. Today* **2023**, *35*, 101959.
[64] D. Tahir, M. Zhang, H. Hu, *Phys. Status Solidi B Basic Res.* **2022**, *259*, 2200324.
[65] R. Xu, C. Chen, J. Sun, X. Wu, Y. Su, J. Shi, X. Li, W. Peng, W. Wu, J. Xiong, Y. Lu, *In. J. Extreme Manufact.* **2023**, *5*, 042013.
[66] S. Shukla, B. K. Behera, *Compos Struct.* **2022**, *290*, 115530.
[67] W. Liu, Y. Zhang, Z. Guo, D. Li, S. Zhao, W. Xie, *Thin-Walled Struct.* **2023**, *192*, 111134.
[68] F. Ciftci, *Process Biochem.* **2024**, *137*, 99.
[69] E. Mohammadi, S. M. Amini, *Nano-Struct. Nano-Objects* **2024**, *38*, 101175.
[70] M. Alhajj, S. K. Ghoshal, *J. Mol. Liq.* **2024**, *414*, 126130.
[71] V. Gaubert, H. Gidik, N. Bodart, V. Koncar, *Sensors* **2020**, *20*, 1739.
[72] Y. Zhu, W. Wang, Y. Zhou, R. Qin, B. Qin, T. Zhou, M. Qiu, Q. Li, *Laser Photon Rev* **2023**, *17*, 2300293.
[73] R. G. Belliveau, S. A. DeJong, N. D. Boltin, Z. Lu, B. M. Cassidy, S. L. Morgan, M. L. Myrick, *Text. Res. J.* **2020**, *90*, 1431.
[74] J. Zhang, H. Dong, Y. Yu, S. Yin, M. Cao, C. Li, X. Shen, J. Li, Y. Xu, S. Chen, F. Xu, *Adv. Funct. Mater.* **2025**, *35*, 2419777.
[75] X. X. Dong, Y. M. Cao, C. Wang, B. Wu, M. Zheng, Y. B. Xue, W. Li, B. Han, M. Zheng, Z. S. Wang, M. P. Zhuo, *ACS Appl. Mater. Interfaces* **2023**, *15*, 12032.
[76] J. F. R. Van Guyse, J. Verjans, S. Vandewalle, K. De Bruycker, F. E. Du Prez, R. Hoogenboom, *Macromolecules* **2019**, *52*, 5102.
[77] J. F. R. Van Guyse, M. N. Leiske, J. Verjans, Y. Bernhard, R. Hoogenboom, *Angew. Chem. Int. Ed.* **2022**, *61*, 202201781.
[78] Y. Bernhard, J. F. R. Van Guyse, M. Purino, R. Hoogenboom, *Eur. Polym. J.* **2023**, *192*, 112077.
[79] J. Verjans, T. Sedlačík, V. V. Jerca, Y. Bernhard, J. F. R. Van Guyse, R. Hoogenboom, *A. C. S. Macro Lett.* **2023**, *12*, 79.
[80] E. Schoolaert, P. Ryckx, J. Geltmeyer, S. Maji, P. H. M. Van Steenberge, D. R. D'hooge, R. Hoogenboom, K. De Clerck, *ACS Appl. Mater. Interfaces* **2017**, *9*, 24100.
[81] J. Mikuła, D. Pakuła, L. Żukowska, K. Gołombek, A. Kříž, *Coatings* **2021**, *11*, 157.
[82] K. Althagafy, F. A. Alamer, *Cellulose* **2025**, *32*, 5709.
[83] J. Antunes, K. Matos, I. Carvalho, S. Carvalho, F. Ferreira, S. M. A. Cruz, *Coatings* **2022**, *12*, 1399.
[84] S. Shahidi, B. Moazzenchi, M. Ghoranneviss, *Euro. Physic. J. Appl. Phys.* **2015**, *71*, 31302.
[85] A. Krella, *Coatings* **2020**, *10*, 921.
[86] H. Gidik, S. Almuhamed, D. Dupont, L. Derue, W. Thielemans, G. Kignelman, D. Lahem, *J. Fashion Technol. Text. Eng.* **2018**, S5:002.
[87] S. H. Yao, Y. L. Su, W. H. Kao, K. W. Cheng, *Surf. Coat. Technol.* **2006**, *201*, 2520.
[88] J. Naeem, A. Mazari, M. S. Naeem, A. Rasheed, F. Ahmad, S. Ahmad, *J. Text. Inst.* **2023**, *114*, 820.
[89] F. J. Sanchez-Marin, S. Calixto-Carrera, C. Villaseñor-Mora, *J. Biomed. Opt.* **2009**, *14*, 024006.
[90] Y. Zhang, S. Furyk, L. B. Sagle, Y. Cho, D. E. Bergbreiter, P. S. Cremer, *J. Phys. Chem. C* **2007**, *111*, 8916.
[91] W. S. P. Carvalho, C. Lee, Y. Zhang, A. Czarnecki, M. J. Serpe, *J. Colloid Interface Sci.* **2021**, *585*, 195.
[92] Y. Zhang, S. Furyk, D. E. Bergbreiter, P. S. Cremer, *J. Am. Chem. Soc.* **2005**, *127*, 14505.
[93] K. Shi, D. Sha, J. D. Xu, X. Yang, B. L. Wang, Y. X. Pan, X. L. Ji, *Chinese J. Poly. Sci.* **2020**, *38*, 257.
[94] B. Kang, H. Tang, Z. Zhao, S. Song, *ACS Omega* **2020**, *5*, 6229.
[95] K. P. Gregory, G. R. Elliott, H. Robertson, A. Kumar, E. J. Wanless, G. B. Webber, V. S. J. Craig, G. G. Andersson, A. J. Page, *Phys. Chem. Chem. Phys.* **2022**, *24*, 12682.
[96] W. Wei, *Adv. Sci.* **2023**, *10*, 2302057.